Activation of Lattice and Adatom Oxygen by Highly Stable Ceria-supported Cu Single Atoms

Authors: Carlos E. García-Vargas[1,2,^], Gregory Collinge[3,^], Dongmin Yun[1], Mal-Soon Lee[3], Valery Muravev[4], Ya-Qiong Su[4], Xavier Isidro Pereira-Hernández[1,3], Dong Jiang[1], Vassiliki-Alexandra Glezakou[3], Emiel J.M. Hensen[4], Roger Rousseau*[3], Abhaya Datye[5], Yong Wang*[1,3]

Affiliations:

[1]The Gene and Linda Voiland School of Chemical Engineering and Bioengineering, Washington State University, Pullman, Washington 99164, United States.

[2]Environmental Molecular Sciences Laboratory, Richland, Washington 99354, United States.

[3]Institute for Integrated Catalysis, Pacific Northwest National Laboratory, Richland, Washington 99354, United States

[4]Laboratory of Inorganic Materials and Catalysis, Department of Chemical Engineering and Chemistry, Eindhoven University of Technology, P.O. Box 513, 5600 MB Eindhoven, The Netherlands

[5]Department of Chemical and Biological Engineering and Center for Micro-engineered Materials, University of New Mexico, Albuquerque, New Mexico 87131, United States.

*Corresponding author. Email: yong.wang@pnnl.gov, roger.rousseau@pnnl.gov

^ These authors contributed equally.

Abstract: Requiring catalysts to be both active yet stable over long periods of time under variable reaction conditions including high and low temperatures is a daunting challenge due to the almost mutual exclusivity of these constraints. Using CO oxidation as a probe reaction, we demonstrate that thermally stable single atom copper catalysts prepared by high temperature synthesis (atom trapping) on ceria can achieve this feat by allowing modulation of the Cu charge state through facile charge transfer between active site and support. This provides the catalysts with an ability to activate either lattice or adatom oxygen atoms, accessing additional reaction channels depending on the reaction conditions. Such adaptability allows dynamic response of catalysts enabling them to remain active under variable reaction conditions. The inherent stability of the catalyst arises from the enhanced strength of the Cu-O interactions from high temperature synthesis that exist even when Cu oxidation state varies, which retards sintering and deactivation. As we show here, one can circumvent the dilemma of designing catalysts that are simultaneously active and stable by matching the redox properties of the active site and support and establishing an environmental adaptability around the active sites.

One Sentence Summary: Thermally stable copper single atom catalysts allow facile charge transfer between the ceria and Cu, by permitting variation of reaction mechanisms with changing reaction conditions, leading to active and stable catalysts.

Main Text:

To achieve catalysts that are both active and stable is particularly challenging for the cleanup of exhaust emissions. Removing harmful CO from exhaust emissions by CO oxidation is a critical challenge for the automotive industry, particularly during cold-start where temperatures are below 150 ºC, under which conditions CO oxidation is commonly prohibitively slow (*1*). This is because CO oxidation is typically accomplished by platinum group metal (PGM) catalysts that are remarkably active at high temperatures but tend to bind CO so strongly at low temperatures that they build up on the surface and block O_2 from being activated for further CO oxidation, effectively halting the reaction (*2*). To overcome this, PGM nanoparticles (NPs) are dispersed on reducible oxide supports in commercial catalysts to maximize the oxide/metal interface (*3*). Such a strategy produces structures that can achieve low temperature CO oxidation through the Mars-van Krevelen (MvK) mechanism, where CO and O_2 are activated on separate sites (metal sites and oxygen vacancies of the support, respectively) (*4*). However, while highly dispersed metallic NPs are active at low temperatures, they are thermally unstable at high temperatures due to agglomeration and sintering, and transformation to an oxide which drastically reduces their low-temperature activity (*5*). High-temperature calcination of highly dispersed Pt NPs (a strategy known as “atom trapping”) produces thermally stable single atom catalysts, but they exhibit poor low temperature activity (*6*). Activation with CO enhances low temperature activity(*7*), but exposure to oxidative conditions at high temperature forms dispersed single atoms that drastically reduce low temperature activity. Adding to these challenges is the scarcity of PGMs —the automotive industry already consumes nearly 50% of global PGM demand (*8*)—it is clear that non-PGM catalysts need to be developed to meet the ever increasing demands of emission control. Surprisingly, preparation of non-PGM Cu_1/CeO_2 by atom trapping produces a catalyst with robust low temperature reactivity that persists even after exposure to high temperatures and reductive/oxidative conditions (*9*, *10*). Here, we provide atomic level understanding of these remarkable properties. Through a fully integrated experimental and theoretical approach, we explain that the rapid shuttling of electrons between Cu and the support during CO oxidation creates a dynamic charge center that allows semi-local control of the mobility of nearby oxygen species crucial for both low and high temperature activity. This results in the intrinsic low-temperature activity of Cu_1/CeO_2, while its thermal stability is achieved through the anchoring of Cu atoms to $CeO_2(111)$ step sites which are able to prevent sintering even at high temperatures.

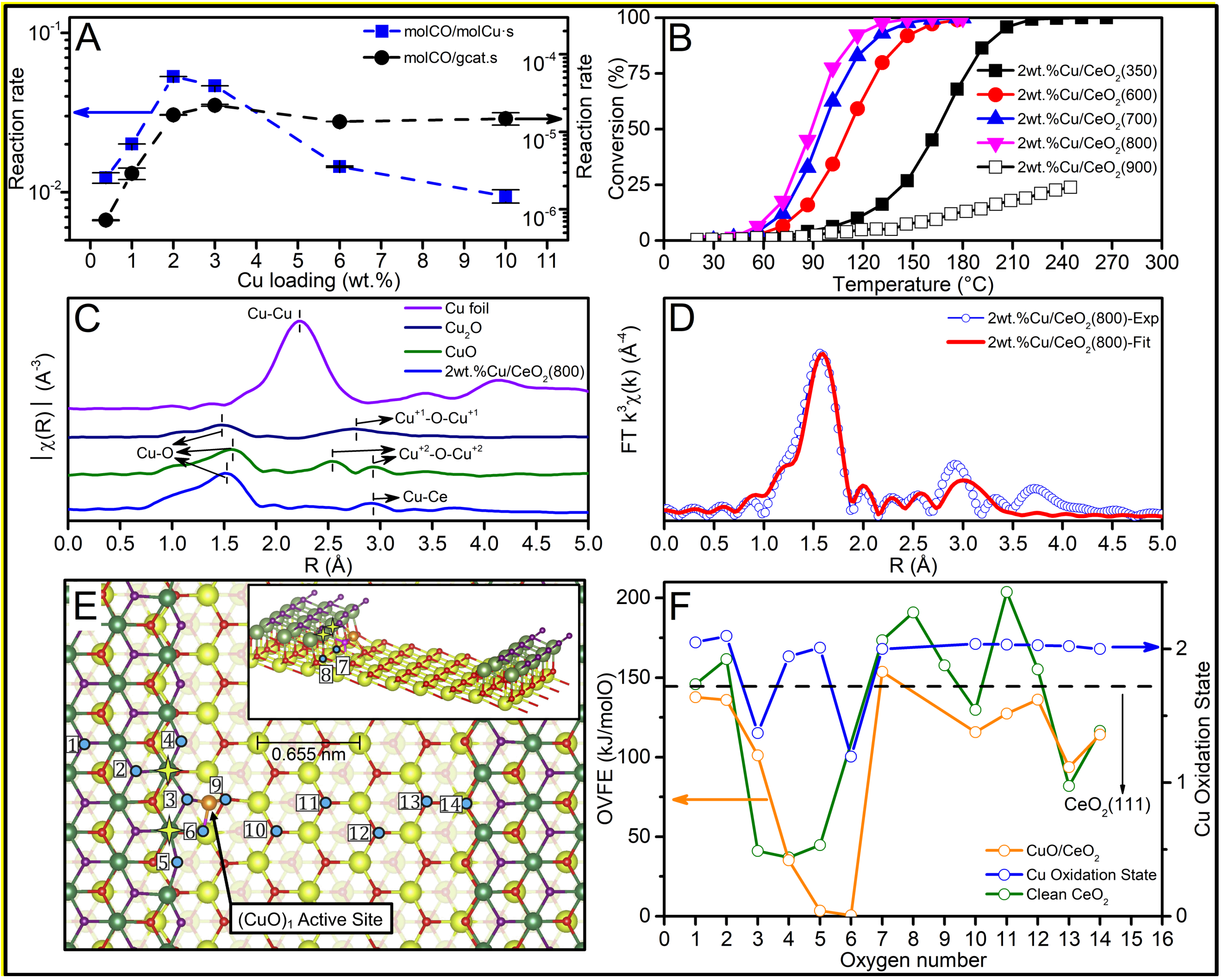

Fig. 1. A) CO oxidation reaction rate normalized by mol of Cu and gram of catalyst for Cu_1/CeO_2 samples calcined at 800 ºC, T = 70 ºC and $X_{CO} < 10\%$: [CO] = 1%; [O_2] = 8%. B) CO oxidation light-off curves for Cu_1/CeO_2 catalysts calcined at temperatures from 350 °C to 900 °C. C) Comparison of experimental EXAFS of 2wt.% Cu_1/CeO_2(800) with Cu foil, Cu_2O, and CuO references. D) Experimental EXAFS and its respective fitting of 2wt.% Cu_1/CeO_2(800) catalyst. E) Top-down view of step-defected Cu_1/CeO_2(111) surface model (Inset: Oblique view). Specific oxygen atoms have been numbered to aid discussion, and the Ce atoms directly above O atoms #7 and #8 have been indicated with yellow stars. Atom legend: dark green = upper terrace Ce, light green = lower terrace and subsurface Ce, purple = upper terrace O of CeO_2, red = lower terrace and subsurface O of CeO_2, orange = Cu, magenta = O of $(CuO)_1$. F) Oxygen vacancy formation energies (OVFEs) (orange & green lines) and resultant Cu oxidation state (blue line) computed for oxygens labeled in Fig. 1E. Note that O atoms #8 and #9 are missing due to instability.

We observed that the reaction rate (mole CO/mole Cu/s) over the Cu_1/CeO_2 catalyst exhibits a pseudo-linear increase in rate as a function of Cu loading up to a maximum at about 2wt.% Cu when calcined at 800°C (Figs. 1A and 1B) while also retaining high surface area (Table S1). The exclusive presence of $(CuO)_1$ single atom centers at 2 wt% and lower loadings was confirmed by sole Cu-O and Cu-Ce contributions in their X-ray absorption fine structure (EXAFS) spectra (Fig.

1C). Absence of bulk or a highly dispersed CuO phase in the EXAFS spectrum was complementarily confirmed by high-angle annular dark-field and scanning transmission electron microscopy (HAADF/STEM) (Figs. S1A and S1B). A positive pseudo-linear relationship between CO oxidation activity and the surface density of single metal atoms was also recently reported for Pd_1/CeO_2 (*11*), where charge shuttling through the ceria support was found to have a cumulative effect on the rate. However, after a critical single atom density the specific rate decreased as Pd NPs began to form. Similarly, we also observe that higher Cu loading coincides with lower reaction rates (in terms of mol CO/mol Cu·s) and the presence of a segregated CuO phase, detected in X-ray diffractograms and EXAFS spectra (Figs. S2A and S2B). In addition, CO light-off curves do not improve at Cu loadings higher than 2wt.% (Fig. S3), suggesting that the CuO phase acts as a spectator during the low-temperature reaction. Agreement between experimental EXAFS and its respective fitting of the 2wt.%Cu_1/CeO_2(800) catalyst (Fig. 1D, Fig. S4 and Table S2) confirms that the molecular model shown in Fig. 1E, derived from a (100) step-defected CeO_2(111) surface (*12*, *13*), reproduces the structural features in this catalyst. Our calculations reveal that strong Cu-O-Ce bonds (>300 kJ/mol/O, Fig. S5, O#3 and O#9 in Fig. 1E) link the Cu^{2+} atom (XANES in Fig. S6) to the top and bottom of the step defect, preventing diffusion and sintering. Further calculations show that oxygen vacancies preferentially form subsurface, but this is reversed by the presence of Cu (Fig. S7). Thus, we can rationalize that high-temperature calcination drives these vacancies to the surface which are filled with O, forming these Cu-O-Ce linkages. At higher Cu loadings (i.e., >2wt.%), however, a computed exothermic driving force (~79 kJ/mol/Cu) easily drives agglomeration and oxidation of unanchored Cu atoms, producing the observed spectator CuO phase (Fig. S8). Higher Cu loading (e.g., 6wt.%) leads to a mixture of $(CuO)_1$ species and CuO spectators as confirmed by the excellent EXAFS fit to our model (Fig. S9A & S9B & Table S3).

As calcination temperature increases from 350 °C to 800 °C, light-off temperatures observed in Fig 1B are improved, which is linked to easier activation of lattice oxygen at lower temperatures, as revealed by CO-TPR (Fig. S10). The sharp drop off in activity corresponding to calcination at 900 °C correlates well with the drastic reduction in surface area to ~5m^2/g and collapse of the ceria structure (Table S4). CO-TPR as a function of Cu loading (Fig. S11) reveals a broad low-temperature peak up to approximately 70 °C regardless of Cu content. Reaction rates normalized to the concentration of the lattice oxygen species remain constant, independent of the Cu content (Fig. S12), which strongly suggests a crucial role of $(CuO)_1$-induced mobile oxygen lattice species in low temperature CO oxidation. Above 2wt.% Cu, reduction peaks associated with CuO formation (*14*) can also be seen in the CO-TPR at ~ 91-100 °C (Fig.S11), in line with EXAFS and X-ray diffraction (XRD) characterization (Figs S2A & S2B). The CO-TPR peak observed at ~130ºC can be assigned to oxygen species (Ce-O) from nearby $(CuO)_1$ centers. Broad high-temperature features (T > 170ºC) are associated with reduction of CeO_2 (Fig. S13). We can therefore conclude that two new types of lattice O are produced by introduction of Cu single atoms: one responsible for low-temperature activity (T ~35-130 ºC) and another responsible for mid-temperature activity (T~130-170 ºC). Any activity above these temperatures is indistinguishable from that of CeO_2.

Our validated model is employed to investigate the molecular identity of these two types of active lattice oxygen. For this we compute oxygen vacancy formation energies (OVFEs) for all types of oxygen present in the model (Fig. 1E), which has 3 lattice O directly bound to Cu ("Cu-O-Ce species"), 4-6 lattice O in close proximity to Cu ("proximal Ce-O species"), and many more lattice O at progressively further distances. The lattice O atoms we investigated are labeled in Fig.

1E, and their OVFEs can be seen in Fig. 1F. The range of effect of $(CuO)_1$ (orange line) is striking: oxygen mobility is notably enhanced, with distances of at least 1.0 nm needed to recover unmodified CeO_2 behavior (Fig. 1E, after ~ O#12). Of all these, three lattice O are far more mobile than the others (labeled O# 4, 5, and 6 in Fig. 1E & 1F): two proximal Ce-O species (O #4 and #5) and one Cu-O-Ce species (O#6). The proximal Ce-O species are both step edge lattice O, but only one (O#4) is accessible to a CO adsorbed to the Cu. Thus, we can posit that the low-temperature active lattice O could correspond to either the Cu-O-Ce species (O#6), which exhibits nearly thermoneutral oxygen vacancy formation, or a proximal Ce-O species (O#4), which is removed at a cost of only ~35 kJ/mol/O. We will therefore construct and test two separate CO oxidation cycles using both of these lattice O species. However, to identify the mid-temperature active lattice O, we must consider the mobility of O at higher temperatures. To do this, we reassess OVFEs of the lattice O again after removing the most labile Cu-O-Ce species (Fig. S5). This reveals that the proximal Ce-O species, while not as mobile as before, are still mobile enough (OVFE of ~83 kJ/mol/O) to be preferentially removed over unmodified CeO_2 (OVFE of ~145 kJ/mol/O). We therefore posit that these proximal Ce-O species correspond to the observed mid-temperature active lattice O—though we must emphasize that both species are likely active under catalytic conditions. Another catalytic cycle will therefore be constructed based on the serial removal of these two species. Finally, since a Cu^{3+} active site has been invoked in the literature (*15*), we also include an additional catalytic cycle that could conceivably form such a species.

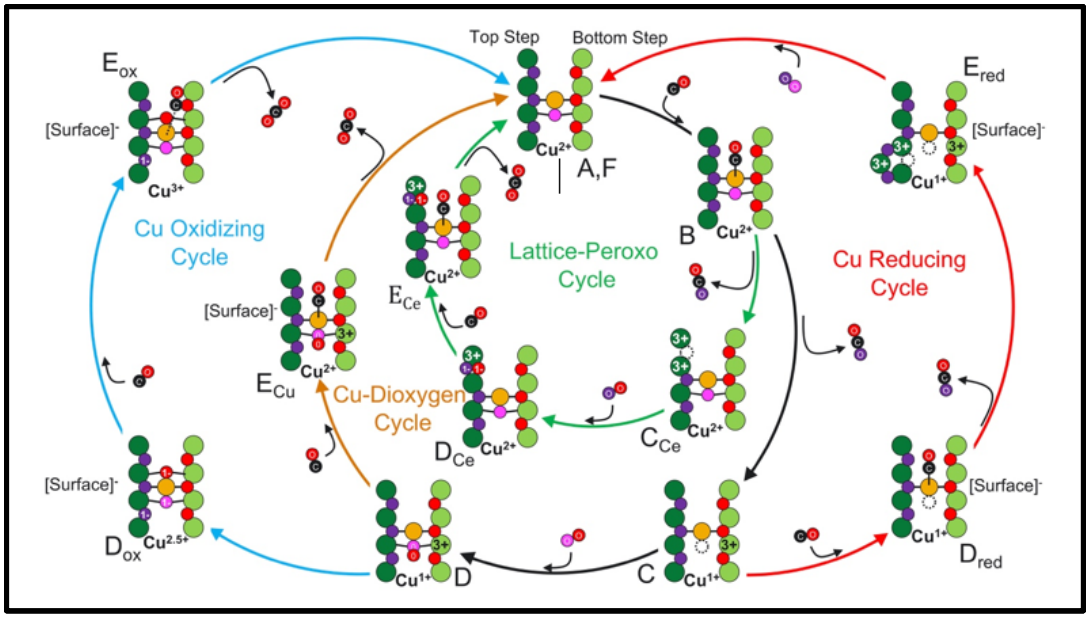

Fig. 2. The four catalytic cycles identified in this work as potentially in operation during CO oxidation. Color coding is identical to that used in Fig. 1E. The formal oxidation state of Cu is shown below each structure (to the nearest 0.5 $|e^-|$). The oxidation state of Ce atoms are 4+ unless noted as "3+"; likewise, O atoms are 2- unless noted as "1-" or "0" (as in dioxygen). Reduction of surface atoms away from Cu are noted with "[surface]-".

The four catalytic cycles are shown in Fig. 2. The two cycles delineated with orange and green lines are built around CO oxidation by Cu-O-Ce species and proximal Ce-O species, respectively.

We term these the “Cu-Dioxygen” and “Lattice-Peroxo” cycles after the location of their lattice O and the identity of the molecular O_2 that subsequently fills the vacancy. The cycle created by two sequential CO oxidation steps involving first the Cu-O-Ce then the proximal Ce-O species results in the reduction of the Cu atom from 2+ to 1+ and is delineated with red lines and termed the “Cu Reducing” cycle accordingly. Finally, if one splits the adsorbed dioxygen across the Cu atom in the Cu-Dioxygen cycle, Cu can be oxidized to 2.5+/3+. This forms our final cycle, the “Cu Oxidizing” cycle, delineated with blue lines. Concurrent with charge transfer in the last two cycles, we have observed that there is facile charge transfer between the support and metal center.

In Fig. 3, we determine adsorption and activation free energies for each elementary step in each aforementioned catalytic cycle. The computed activation free energy/intrinsic activation energy is presented for comparison against the experimentally measured apparent activation energies for the 0.37, 1.0, and 2.0wt.% Cu/CeO_2 samples (Fig. 3E). The highest barriers (and, if ambiguous, their competitiveness against CO desorption) were used to identify likely rate determining steps (RDS) for each cycle, with the structure preceding each RDS making up the putative most abundant surface intermediate (MASI) of that cycle. The Cu-Dioxygen cycle (Fig. 3A) exhibits the lowest overall barriers, and its RDS has an intrinsic activation energy of ~54 kJ/mol, which is in remarkable agreement with the experimentally determined value (~55 kJ/mol) for the lowest Cu loading sample (0.37wt.% Cu) where fully isolated single Cu atom sites are most guaranteed. This is strong evidence that low-temperature CO oxidation over Cu_1/CeO_2 proceeds primarily via the Cu-Dioxygen cycle. Splitting dioxygen (structure D in Fig. 2) to enter the Cu Oxidizing cycle is kinetically inhibited (computed barrier of 146 kJ/mol) despite being exothermic (ΔG_{rxn} = -80 kJ/mol). Any Cu^{3+} single atom sites formed prior to reaction will therefore very seldom reform, making the Cu Oxidizing cycle likely inactive until much higher temperatures. The Lattice-Peroxo and Cu-Reducing cycles are competitive with each other, each having a different RDS but a similar forward barrier (~ 95-97 kJ/mol). These two cycles are therefore most likely involved in the mid-temperature range, and an increased flux through these pathways as Cu_1 loading is increased would be consistent with the measured increase in apparent activation energy to ~70 kJ/mol. We should note, however, that despite recent reports (*10*), we see no evidence that an Eley-Rideal mechanism between molecular O_2 and bound CO is in play.

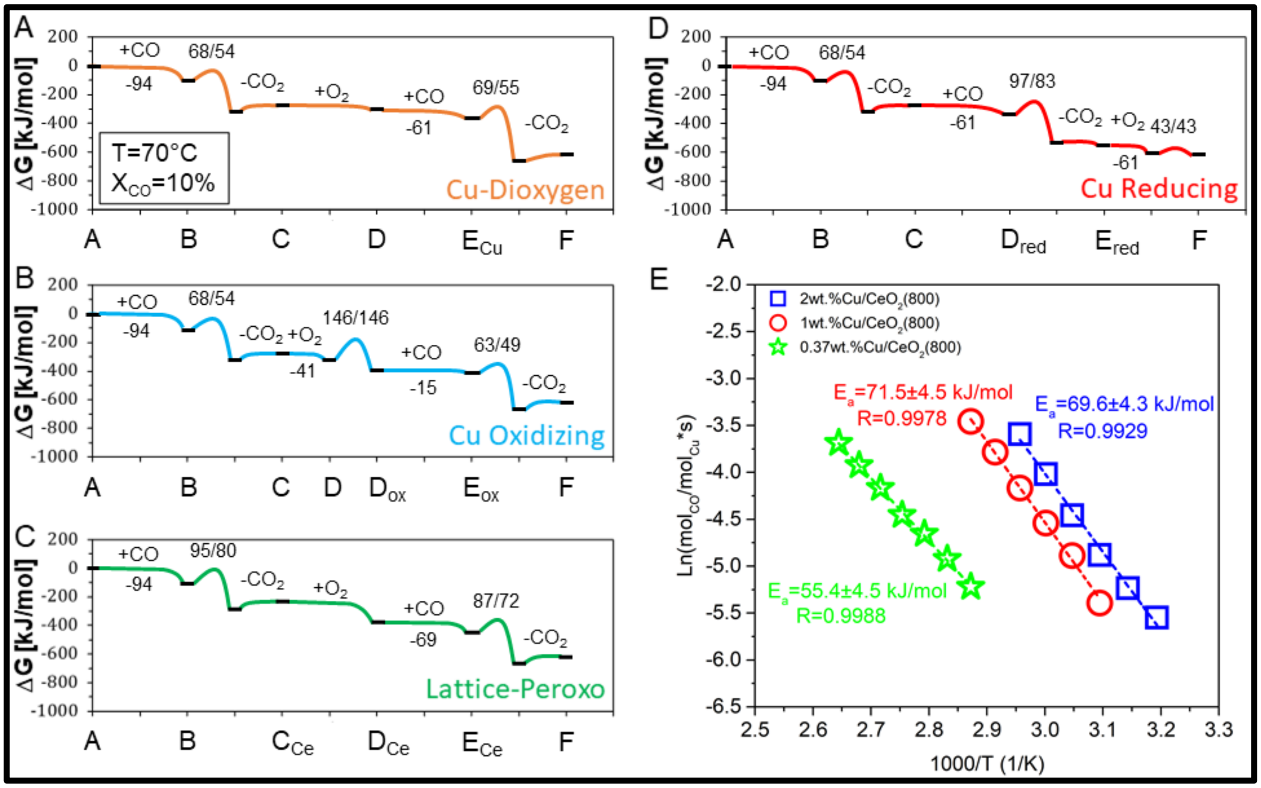

Fig. 3. Computed (T=70 ºC and X_{CO}=10%) free energy diagrams for the A) Cu-Dioxygen cycle, B) the Cu Oxidizing cycle, C) the Lattice-Peroxo cycle, and D) the Cu Reducing Cycle. E) Experimental Arrhenius plots of Cu_1/CeO_2 calcined at 800 °C with 2wt.%, 1wt.% and 0.37wt.% Cu loading taken at X_{CO}<10%.

We used ambient-pressure X-ray photoelectron spectroscopy (AP-XPS) to probe and test the theoretically predicted charge states during low temperature CO oxidation. As seen in Fig. 4A, under CO oxidizing conditions, only Cu^{2+} is detected—in agreement with our XANES results. While mostly Ce^{4+} is detected, a small amount of Ce^{3+} can be seen. If the Cu-Dioxygen cycle is in operation during low-temperature CO oxidation, then Structure B (exhibiting CO adsorbed to Cu^{2+}, CO-Cu^{2+}) should be the MASI, but this structure displays no Ce^{3+}. However, the next MASI along the Cu-Dioxygen cycle is Structure E_{Cu}, which still exhibits Cu^{2+} but with some Ce^{3+} present. A small representation of Structure E_{Cu} amongst a MASI of otherwise Structure B is therefore consistent with the AP-XPS results. We also consider what might happen if O_2 is cut off from the reaction (CO-only conditions). In this scenario, the MASI should still be primarily Structure B, but the lowest barrier pathway forward without O_2 is to progress to Structure C and proceed specifically into the Cu reducing cycle. Under low-temperature conditions, the reaction should largely stop at Structure D_{red} due to a ~97 kJ/mol forward barrier that exhibits Cu^{1+} and Ce^{3+}. This theoretical prediction is born out experimentally. Once O_2 is removed from the sample, AP-XPS spectra exhibit a noticeable uptick in $Cu^{1+/0}$ and Ce^{3+}, with the fraction of $Cu^{1+/0}$ present estimated at 0.15 [Table S5].

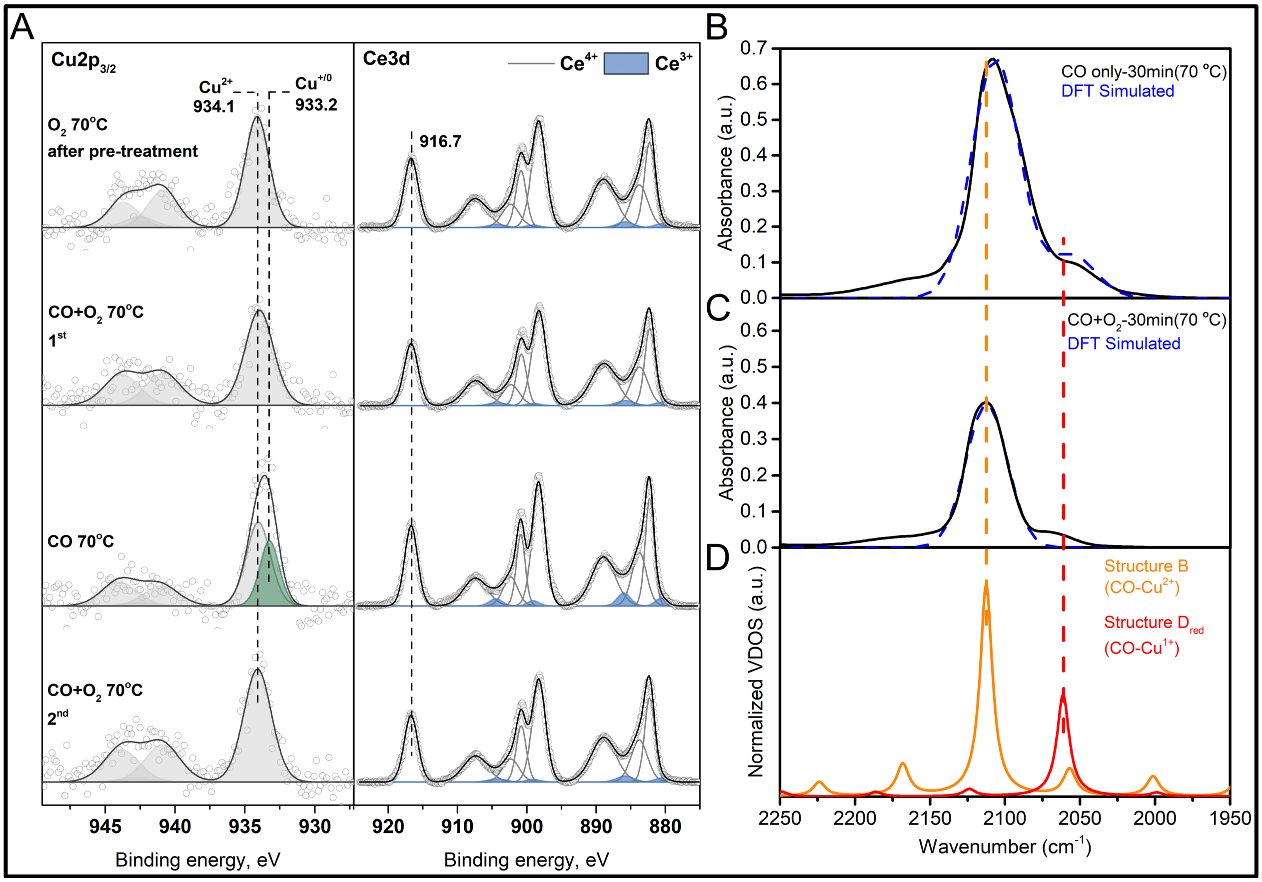

Fig. 4. a) Cu 2p and Ce 3d ambient-pressure X-ray photoelectron spectra (AP-XPS) of 2wt.%Cu$_1$/CeO$_2$ made by calcination at 800 C. b) Experimental diffuse reflectance infrared Fourier transform spectroscopy (DRIFTS) spectra (black lines) of the Cu$_1$/CeO$_2$ catalyst vs. the corresponding density functional theory (DFT)-simulated DRIFTS (dashed blue lines), under (a) a CO only atmosphere and (b) a CO oxidizing atmosphere. (d) Normalized VDOS peaks derived from AIMD of structure B (orange) and structure Dred (red).

The MASIs in question here are Structure B (CO-Cu^{2+}) and Structure D$_{red}$ (CO-Cu^{1+}), each containing an adsorbed CO on Cu^{2+} or Cu^{1+}. If our assignments are truly correct, then the computed CO stretch frequencies for these two structures should match the predictions made from AP-XPS and analysis of the catalytic cycles. To ensure the most accurate computed values possible, ab initio molecular dynamics (AIMD) simulations on each MASI structure were performed at 70°C to extract *anharmonic* (*16*) CO stretch frequencies in the form of CO vibrational density of states (CO-VDOS) (see Supplementary Information for details). Diffuse reflectance infrared Fourier transform spectroscopy (DRIFTS) was then independently performed at 70 ºC under CO oxidizing and CO-only conditions. The results are shown in Fig. 4B. Under CO oxidizing conditions (prediction: ~100% CO-Cu^{2+}), DRIFTS detects one primary peak at 2112 cm^{-1}. Under CO only (prediction: ~85% CO-Cu^{2+} and ~15% CO-Cu^{1+}), this peak red shifts slightly to ~2108 cm^{-1}, and a clear shoulder develops around the 2050 cm^{-1} region. The computed CO-VDOS for CO-Cu^{2+} (Structure B) is centered at 2112.5 cm^{-1}, in very good agreement with the primary DRIFTS peaks under both sets of conditions. The CO-VDOS for CO-Cu^{1+} (Structure D$_{red}$) is centered at 2061 cm^{-1}, which aligns very well with the shoulder developed under CO-only conditions. In the Cu$_1$/CeO$_2$ system, the 2050 cm^{-1} feature has never been assigned to any Cu-CO species, whereas the 2110 cm^{-1} species has been widely attributed to CO-Cu^{1+}, but such attribution has apparently been derived from imprecise extrapolation of Cu-CO assignments from Cu/SiO$_2$, Cu^0, and Cu/Al$_2$O$_3$ (Table S6). To visually compare the identified Cu-CO species in this work, we construct a DFT-simulated DRIFTS spectra by applying Gaussian functions to each primary CO VDOS peak weighted according to the fraction of Cu^{2+} (0.85) and Cu^{1+} (0.15) that are predicted to be present under CO only conditions according to AP-XPS (Table S5). The same process was applied to a single Gaussian centered around the primary CO VDOS peak at 2112.5 cm^{-1} to compare against the DRIFTS under CO oxidizing conditions. The y-scales were adjusted to align peak maxima. This leaves no tunable parameters that could otherwise be used to perform a fitting. The resultant DFT simulated spectra are shown as dotted blue lines for CO only and CO oxidizing conditions in Fig. 4B. The overall shape and placement of each DFT simulated spectra are consistent with the experiment. In fact, a 6 cm^{-1} red shift, applied to the entire DFT simulated spectrum in Fig. 4B, is sufficient to produce a nearly perfect match (Fig. S14). Such a shift could easily be the result of ensemble effects not accounted for in the model. This demonstrates that the flexible charge transfer observed above contributes to the ability of the catalyst to adapt to the reaction environment and remain active.

We have conclusively shown here that low temperature CO Oxidation over Cu$_1$/CeO$_2$ proceeds via Cu single atom active sites trapped at step defects, with Cu-O-Ce being the primary active oxygen species. We show that Cu cycles between 2+ and 1+ oxidation states during its primary catalytic cycle with mostly CO-Cu^{2+} making up the MASI. It is especially interesting to note that as temperatures increase, other catalytic cycles will contribute to the reaction. The considerable debate in the literature concerning the active site of Cu$_1$/CeO$_2$ for CO oxidation can potentially be understood as a reflection of this concert of catalytic cycles producing a wide distribution of surface structures and potential charge states. Finally, we show that the remarkable robustness of this catalyst results from its ability to adapt to changes in thermodynamic conditions whilst always manifesting a viable low temperature route for CO oxidation.

References

1. M. Zammit, C. Dimaggio, C. Kim, C. Lambert, G. Muntean, C. Peden, J. Parks, K. Howden, “Future Automotive Aftertreatment Solutions : The 150 °C Challenge Workshop Report” (2012).

2. J. Liu, F. R. Lucci, M. Yang, S. Lee, M. D. Marcinkowski, A. J. Therrien, C. T. Williams, E. C. H. Sykes, M. Flytzani-Stephanopoulos, Tackling CO Poisoning with Single-Atom Alloy Catalysts. *J. Am. Chem. Soc.* **138**, 6396–6399 (2016).

3. A. Beniya, S. Higashi, Towards dense single-atom catalysts for future automotive applications. *Nat. Catal.* **2**, 590–602 (2019).

4. S. Royer, D. Duprez, Catalytic Oxidation of Carbon Monoxide over Transition Metal Oxides. *ChemCatChem*. **3**, 24–65 (2011).

5. C. Carrillo, A. Delariva, H. Xiong, E. J. Peterson, M. N. Spilde, D. Kunwar, R. S. Goeke, M. Wiebenga, S. H. Oh, G. Qi, S. R. Challa, A. K. Datye, Regenerative trapping: How Pd improves the durability of Pt diesel oxidation catalysts. *Appl. Catal. B Environ.* **218**, 581–590 (2017).

6. D. Kunwar, S. Zhou, A. De La Riva, E. Peterson, H. Xiong, X. Isidro Pereira Hernandez, S. C. Purdy, R. ter Veen, H. H. Brongersma, J. T. Miller, H. Hashiguchi, L. Kovarik, S. Lin, H. Guo, Y. Wang, A. Datye, A. DeLaRiva, E. J. Peterson, X. Isidro Pereira Hernández, A. K. Datye, Stabilizing High Metal Loadings of Thermally Stable Platinum Single Atoms on an Industrial Catalyst Support. *ACS Catal.* (2019), doi:10.1021/acscatal.8b04885.

7. X. I. Pereira-Hernández, A. DeLaRiva, V. Muravev, D. Kunwar, H. Xiong, B. Sudduth, M. Engelhard, L. Kovarik, E. J. M. Hensen, Y. Wang, A. K. Datye, Tuning Pt-CeO2 interactions by high-temperature vapor-phase synthesis for improved reducibility of lattice oxygen. *Nat. Commun.* **10**, 1358 (2019).

8. C. Hagelüken, M. Buchert, H. Stahl, Substantial Outflows of Platinum Group Metals Identified: Spent Autocatalysts are Systematically Withdrawn from the European Market. *ERZMETALL*. **56**, 529–540 (2003).

9. R. Alcala, A. DeLaRiva, E. J. Peterson, A. Benavidez, C. E. Garcia-Vargas, D. Jiang, X. I. Pereira-Hernández, H. H. Brongersma, R. ter Veen, J. Staněk, J. T. Miller, Y. Wang, A. Datye, Atomically Dispersed Dopants for Stabilizing Ceria Surface Area. *Appl. Catal. B Environ.* **284**, 119722 (2021).

10. W.-Z. Yu, W.-W. Wang, S.-Q. Li, X.-P. Fu, X. Wang, K. Wu, R. Si, C. Ma, C.-J. Jia, C.-H. Yan, Construction of active site in a sintered copper-ceria nanorod catalyst. *J. Am. Chem. Soc.* **141**, 17548–17557 (2019).

11. Y. Kim, G. Collinge, M. S. Lee, K. Khivantsev, S. J. Cho, V. A. Glezakou, R. Rousseau, J. Szanyi, J. H. Kwak, Surface Density Dependent Catalytic Activity of Single Palladium

Atoms Supported on Ceria**. *Angew. Chemie Int. Ed.* **60**, 22769–22775 (2021).

12. N. Nilius, S. M. Kozlov, J. F. Jerratsch, M. Baron, X. Shao, F. Viñes, S. Shaikhutdinov, K. M. Neyman, H. J. Freund, Formation of One-dimensional electronic states along the step edges of CeO 2(111). *ACS Nano*. **6**, 1126–1133 (2012).

13. J. L. Lu, H. J. Gao, S. Shaikhutdinov, H. J. Freund, Morphology and defect structure of the CeO2(1 1 1) films grown on Ru(0 0 0 1) as studied by scanning tunneling microscopy. *Surf. Sci.* **600**, 5004–5010 (2006).

14. T. Caputo, L. Lisi, R. Pirone, G. Russo, On the role of redox properties of CuO/CeO2 catalysts in the preferential oxidation of CO in H2-rich gases. *Appl. Catal. A Gen.* **348**, 42–53 (2008).

15. J. S. Elias, K. A. Stoerzinger, W. T. Hong, M. Risch, L. Giordano, A. N. Mansour, Y. Shao-Horn, In Situ Spectroscopy and Mechanistic Insights into CO Oxidation on Transition-Metal-Substituted Ceria Nanoparticles. *ACS Catal.* **7**, 6843–6857 (2017).

16. G. Collinge, S. F. Yuk, M. T. Nguyen, M. S. Lee, V. A. Glezakou, R. Rousseau, Effect of Collective Dynamics and Anharmonicity on Entropy in Heterogenous Catalysis: Building the Case for Advanced Molecular Simulations. *ACS Catal.* **10** (2020), pp. 9236–9260.

Acknowledgments:

Funding: Research has been funded by the US Department of Energy (DOE), Office of Science, Office of Basic Energy Sciences, Chemical Sciences, Geosciences and Biosciences Division, Catalysis Program under FWP 47319 (computational studies) and DOE Energy Efficiency and Renewable Energy, Vehicle Technology Office under FWP 45851 (experimental studies). Computer resources were provided by the National Energy Research Center (NERSC), a U.S. Department of Energy, Office of Science User Facility located at Lawrence Berkeley National Laboratory and Research Computing facility located at the Pacific Northwest National Laboratory (PNNL). PNNL is operated by Battelle for DOE.

Author contributions: Experiments were performed by CGV, DY, VM, YQS, XIPH and DJ with computations performed by GC and MSL. All authors collaborated on the design of the research and preparation of the manuscript.

Competing interests: Authors declare no competing interests

Data and materials availability: All data is available in the main text or the supplementary materials.

Supplementary Materials:

Materials and Methods

Figs. S1-S16

Tables S1-S6

References (1-16)

Appendix S1: Structural data